Journal of Materials Chemistry A

PAPER

View Article Online
View Journal | View Issue

Cite this: J. Mater. Chem. A, 2017, 5, 9760

Atomic layer deposited tantalum oxide to anchor Pt/C for a highly stable catalyst in PEMFCs†

Zhongxin Song,[a] Biqiong Wang,[a] Niancai Cheng,[a] Lijun Yang,[b] Dustin Banham,[b] Ruying Li,[a] Siyu Ye*[b] and Xueliang Sun *[a]

Received 2nd March 2017
Accepted 13th April 2017

DOI: 10.1039/c7ta01926b

rsc.li/materials-a

Tantalum oxide (TaO_x) nanoparticles (NPs) are deposited on a commercial Pt/C catalyst by an area-selective atomic layer deposition (ALD) approach to enhance the stability of the catalyst in proton exchange membrane fuel cells (PEMFCs). Due to the application of a blocking agent for protecting the Pt surface, TaO_x particles are selectively nucleated and grown around Pt NPs. The TaO_x loading on the Pt/C surface could be controlled precisely by varying the number of ALD cycles. When deposited on the Pt/C surface with 35 ALD cycles, the TaO_x-anchored Pt NPs formed an excellent triple-junction structure of TaO_x–Pt–carbon. The electrochemical durability tests indicated that the TaO_x-anchored Pt/C catalyst showed comparable catalytic activity and superior long-term stability to Pt/C. Moreover, the long-term stability test in membrane electrode assembly (MEA) indicated a very low power density loss (12%) after a 120 h accelerated durability test. The significantly enhanced catalyst stability during PEMFCs operation is due to the anchoring effect of TaO_x *via* strong metal oxide–support interactions. This strategy shows great potential for developing highly stable catalysts for PEMFCs.

Introduction

Fuel cells, especially proton exchange membrane fuel cells (PEMFCs), are considered as a new energy technology with potential applications in power demanding areas such as electronic vehicles, automobiles and distributed stationary power sources.[1–3] As a crucial component of PEMFCs, Pt-based catalysts are used to catalyse chemical reactions in PEMFCs (hydrogen oxidation at the anode and oxygen reduction at the cathode) for promoting electrochemical energy conversion.[4–9] However, the high cost and poor durability of Pt catalysts severely hamper the practical commercialization of such electrochemical devices.[10,11] This is because the catalysts must survive thousands of load cycles over the lifetime of PEMFC operation under harsh conditions, such as high temperature and potential, low pH, and oxygen atmosphere.[12,13] In such an environment, Pt catalysts undergo significant degradation and performance loss due to Pt nanoparticles (NPs) dissolution, migration/coalescence, Ostwald ripening and detachment from the carbon support. Therefore, improving the durability of Pt catalysts has been one of the most important issues.

In order to overcome the durability problems, numerous research efforts have been made to enhance the stability of Pt catalysts by endowing Pt NPs with new morphologies (*e.g.* nanowires, nanotubes, and nanodendrites),[14–19] integrating Pt with other transition metals (Pt/M core–shell, alloy and nanoframe structures),[7,20–22] or developing durable catalyst supports with high corrosion-resistance and strong catalyst–support interactions (Pt–NGR, Pt–NCNTs, Pt–ZrC, Pt–CeO_2).[9,23–26] Recently, anchoring Pt NPs on carbon supports by means of polymers,[27–29] ultrathin carbon layers,[30] or inorganic materials[31–33] to fabricate immobilized Pt catalysts has shown to be a promising method for stabilizing Pt NPs. There have also been several reports about loading metal oxides on Pt catalysts to improve their activity and durability.[31,34,35] Group IV and V compounds based on the elements Zr, Nb and Ta, mainly nitrides and oxides, have been used as ORR catalysts, owing to their high chemical stability in an acidic environment.[36,37] TaO_x received considerable attention as alloying additives that enhance the activity and durability for various catalysts.[38] For instance, Bonakdarpour *et al.* found that Ta addition markedly enhances the durability and reduces the dissolution of Pt in the sputtered Pt/Ta alloy ORR catalyst by forming a thin Ta_2O_5 passivation layer.[39] Kazunari Domen *et al.*[40–43] reported that the ultrafine designed TaO_x nanoparticles, by electrodeposition as an electrocatalyst for ORR, showed excellent catalytic activity. Recently, Takeo Ohsaka *et al.*[44] demonstrated a unique structure of TaO_x-capped Pt NPs on a Pt/TaO_x/GC electrocatalyst. It was found that the amorphous TaO_x of the Pt/TaO_x/GC electrocatalyst caused enhancement of ORR activity and durability, which was due to the spillover effect and the strong interaction between Pt and TaO_x. However, the methods used in these

[a]Department of Mechanical and Materials Engineering, University of Western Ontario, London, N6A 5B9, Canada. E-mail: xsun@eng.uwo.ca

[b]Ballard Power Systems Inc., Burnaby, British Columbia, V5J 5J8, Canada. E-mail: siyu.ye@Ballard.com

† Electronic supplementary information (ESI) available. See DOI: 10.1039/c7ta01926b

reports have a number of limitations, such as the loading amount of TaO_x, local control and the synthesis yields of catalysts for practical PEMFC applications. Another challenge is to design and optimize the metal oxide–Pt structure without reducing the catalyst electrochemical surface area. In order to address the stability issues of Pt catalysts in PEMFCs, atomic layer deposition (ALD) is gaining increasing attention as a technique for preparing noble metals or metal oxides, because of its advantages in developing ultrathin films and uniformly distributed particles in a subnanometer controllable growth process.[45–48] ALD processes are self-limiting surface reactions. Thus, the surface functional groups can be manipulated prior to ALD to carry out an area-selective ALD process.[49,50] For an area-selective ALD method, the desirable material can be deposited where needed without blocking the surface of the catalysts. For instance, N. Cheng *et al.*[51] demonstrated an area-selective ALD approach to stabilize Pt NPs using ALD zirconia nanocages. The Pt NPs catalyst encapsulated in zirconia nanocages exhibited much more stability than Pt–carbon nanotubes without zirconia nanocages.

In this study, we propose a facile area-selective ALD approach to stabilize the Pt/C catalyst through fabricating TaO_x-anchored Pt NPs with the triple-junction structure of Pt–TaO_x–C. By introducing a protective agent (oleylamine) to the Pt surface, TaO_x nanoparticles were selectively nucleated and grown around Pt NPs and formed TaO_x anchored-Pt NPs on the carbon surface. The electrochemical durability tests indicated that the 35ALD–TaO_x–Pt/C catalyst exhibited superior durability compared to Pt/C. The enhanced stability of the 35ALD–TaO_x–Pt/C catalyst is attributed to the anchoring effect of TaO_x *via* the strong triple-junction of TaO_x–Pt–C, which plays a significant role in stabilizing the Pt catalyst by preventing Pt NPs from migration/coalescence and detachment from the carbon support.

Experimental

Area-selective ALD of TaO_x on the Pt/C catalyst

100 mg of the commercial Pt/C catalyst (Tanaka Kikinzoku Kogyo TEC10E50E, with 50 wt% Pt on high surface area carbon black) was suspended in 50 ml ethanol solution and sonicated for 30 min. The dispersed Pt/C solution and 2 ml oleylamine were mixed and then stirred for 5 h. After filtration, washing, and drying under vacuum, oleylamine modified Pt/C (denoted as OA–Pt/C) was obtained. The area-selective deposition of TaO_x on OA–Pt/C was carried out in an ALD reactor (Savannah 100, Cambridge Nanotechnology Inc., USA) at 225 °C using tantalum(v) ethoxide ($Ta(OC_2H_5)_5$) and H_2O as precursors, and N_2 as the carrier gas.[52] The prepared sample will be designated as TaO_x–OA–Pt/C, hereafter. One ALD cycle consists of the following six steps: (1) 0.5 s pulse of $Ta(OC_2H_5)_5$; (2) a 3.0 s extended exposure to $Ta(OC_2H_5)_5$ in the reaction chamber; (3) a purging time of 16 s; (4) 1.0 s pulse of H_2O; (5) a 3.0 s extended exposure to H_2O in the reaction chamber; (6) 25 s purging time. As reported in our previous work,[52] there is a linear relationship between the $LiTaO_x$ film thickness and TaO_x subcycle number. The growth per cycle of TaO_x deposition is ~0.5 Å per cycle, much close to that (~0.4 Å per cycle) reported in another literature study.[53] This confirms that TaO_x was synthesized by an ALD process. The TaO_x loading on Pt/C was accurately controlled by the number of ALD cycles. After ALD processes, the oleylamine in TaO_x–OA–Pt/C samples was removed by heating at 700 °C in an Ar/H_2 atmosphere for 1 h, and the final catalyst is denoted as ALD–TaO_x–Pt/C. In this work, samples of 15ALD–TaO_x–Pt/C, 35ALD–TaO_x–Pt/C, and 50ALD–TaO_x–Pt/C loaded with 15, 35, and 50 ALD cycles of TaO_x were prepared, and the TaO_x loading was 7.8 wt%, 10.2 wt% and 13.5 wt%, tested by energy dispersive X-ray spectroscopy (EDS), respectively. To investigate the TaO_x particle size, the 35ALD–TaO_x–CB sample with 35 ALD cycles of TaO_x on carbon black was also prepared.

Physical characterization

The morphology and microstructures of samples were characterized by using high-resolution TEM (HRTEM, JEOL 2010FEG) and scanning transmission electron microscopy (STEM) with energy dispersive X-ray spectroscopy (EDS). X-ray diffraction (XRD) patterns were collected on a Bruker D8 Advance diffractometer using Cu Kα radiation at 40 kV and 40 mA. The chemical compositions of TaO_x were investigated by X-ray photoelectron spectroscopy (XPS, Kratos Axis Ultra-spectrometer).

Electrochemical characterization

The electrochemical characterizations were conducted in a three-compartment electrochemical cell using a rotating-disk electrode (RDE) setup with an Autolab electrochemistry station and rotation control (Pine Instruments). Catalyst inks were prepared by mixing 3 mg of the catalyst, 3 ml of an 80 : 20 (wt/wt) mixture of ethanol to ultra-pure H_2O, and 30 μl of Nafion (5 wt%). The mixture was then sonicated to ensure good dispersion and wetting of the catalyst. 20 μl of the catalyst ink was deposited onto a polished glassy carbon electrode (Pine, AFE5T050AUHT, 5.0 mm dia.) and allowed to dry at room temperature. All electrochemical measurements were carried out in 0.1 M $HClO_4$ electrolyte using a Pt wire as the counter electrode and a reversible hydrogen electrode (RHE) as a reference electrode. All potentials reported henceforth are *vs.* RHE. Each electrode was activated by cycling from 0.05 to 1.1 V at 50 mV s^{-1} in N_2-saturated 0.1 M $HClO_4$ until no changes were observed in the cyclic voltammetry curves (CV curves). CV curves were recorded by scanning from 0.05 V to 1.1 V at 50 mV s^{-1} in N_2. O_2 was then bubbled for 30 min to achieve an O_2-saturated electrolyte. Oxygen reduction reaction (ORR) linear sweep voltammetry (LSV, 10 mV s^{-1}) was conducted in O_2-saturated 0.1 M $HClO_4$ on the RDE system with a rotation speed of 1600 rpm. The CV curves obtained under N_2 were subtracted from the CV curves obtained under O_2 to remove the non-Faradaic current. The electrochemically active surface area (ECSA) was calculated by integrating the area of the CV curves in the hydrogen underpotential deposition (HUPD) region and using the charge value of 210 μC cm^{-2} corresponding to a monolayer adsorption of hydrogen atoms on a polycrystalline Pt catalyst.[54]

To investigate the impact of potential cycling on catalyst degradation, two aging protocols of accelerated durability tests (ADTs) were performed. (i) PEMFC load-cycling protocol, where

the electrode potential was modulated with a triangle wave from 0.6 to 1.0 V *vs.* RHE at a scan rate of 50 mV s^{-1} in a N_2-saturated 0.1 M $HClO_4$ electrolyte. A total of 10 000 cycles were performed in the "degradation cell" and intermediate characterizations were recorded to monitor the ECSA and mass activity losses. (ii) A start-up/shutdown ADT protocol, where the electrode potential was cycled with a triangle wave from 1.0 V to 1.6 V *vs.* RHE with a scan rate of 100 mV s^{-1} in a N_2-saturated 0.1 M $HClO_4$ electrolyte. A total of 6000 cycles were performed and intermediate characterizations were recorded to monitor the ECSA and mass activity losses.[55]

Membrane electrode assembly (MEA) fabrication and single fuel cell testing

The fuel cell performance of the 35ALD–TaO_x–Pt/C catalyst as a cathode was tested in a single cell system. The MEA with an active area of 45 cm^2 was fabricated by a catalyst-coated membrane (CCM) method. Prior to fabricating the CCM and MEA, a homogeneous catalyst ink was prepared by mixing the 35ALD–TaO_x–Pt/C catalyst, Nafion (10 wt%) and ultrapure water. The as-prepared ink was coated on a Nafion® 211 membrane (25 μm thickness, DuPont Co.) and dried in air at room temperature. Then the anode catalyst layer was decal transferred onto the other side of the Nafion® 211 membrane by hot-pressing. Finally, the CCM was sandwiched between two gas diffusion layers using the Kapton frame with an active area of 45 cm^2. Pt loadings at the anode/cathode side are 0.1/0.15 mg cm^{-2}, respectively. For MEA performance evaluation, the operating conditions were 75 °C, 136 kPa, and 100% relative humidity (RH). Prior to testing, MEA conditioning was performed at the current density of 1.3 A cm^{-2} for 16 h, at 75 °C, 136 kPa, and 100% RH. MEA durability testing was performed at 80 °C, 136 kPa, loaded with a square wave and stepped potential cycling of 0.6 V and 1.0 V holding 30 s at each potential. A total of 4700 cycles (around 120 h) were performed on MEA and intermediate air polarization curves were recorded to monitor the cell voltage and peak power density losses.

Results and discussion

Structural characterization

Scheme 1 demonstrates a facile approach to construct anchored Pt NPs by area-selective deposition of TaO_x on the commercial Pt/C catalyst. Due to the application of a blocking agent (oleylamine) for protecting the Pt surface, TaO_x particles were selectively grown beside the Pt NPs and formed TaO_x-anchored Pt NPs supported on the surface of carbon. The construction of TaO_x anchors with triple junctions of TaO_x–Pt–C was intended to enhance the catalyst durability while not reducing the activity. To investigate the potential trade-off between durability enhancement and activity loss, ALD cycles of 15, 35, and 50 were evaluated to generate protective TaO_x anchors with a progressively increasing amount on the Pt/C matrix.

The morphology and structure of the as-prepared ALD–TaO_x–Pt/C catalysts were characterized by using HRTEM. HRTEM images in Fig. 1(a)–(c) indicate that the TaO_x nanoparticles were successfully deposited on the surface of Pt/C. Increasing the number of ALD cycles leads to high TaO_x coverage on the Pt/C matrix. After 15 ALD cycles (Fig. 1(a) and S1†), only 7.8 wt% TaO_x could be deposited on the surface of Pt/C (based on EDS), and the resulting particles were too small to be viewed by HRTEM, while with 35 ALD cycles of TaO_x deposition, the increased TaO_x loading (10.2 wt%) led to a larger coverage area of TaO_x on the Pt/C surface compared to 15ALD–TaO_x–Pt/C. Fig. S2† shows that TaO_x particles with an average particle size of 2.7 ± 0.5 nm could be uniformly distributed on the carbon support. The STEM image and line scan spectra in Fig. 1(e) and (f) also indicate that the TaO_x nanoparticles are

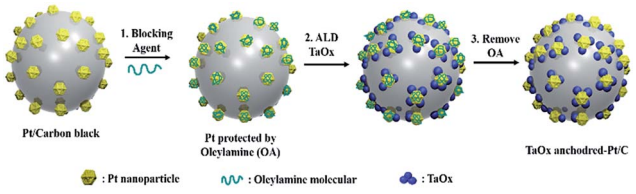

Scheme 1 Schematic illustrations of TaO_x-anchored Pt NPs *via* area-selective atomic layer deposition (ALD).

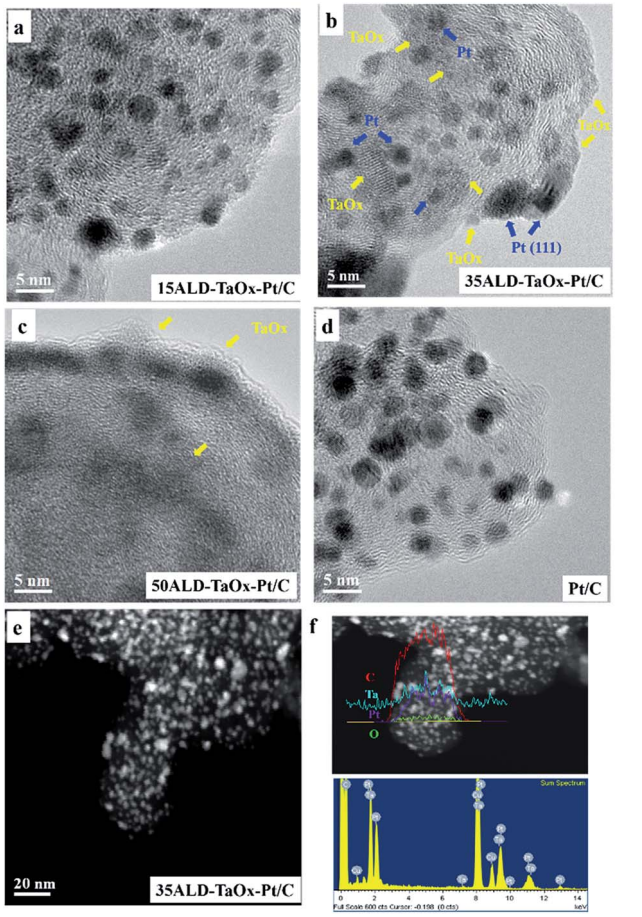

Fig. 1 (a–d) HRTEM images of different catalysts: (a) 15ALD–TaO_x–Pt/C, (b) 35ALD–TaO_x–Pt/C, (c) 50ALD–TaO_x–Pt/C and (d) Pt/C (e and f) STEM image and STEM line scan spectra of the 35ALD–TaO_x–Pt/C catalyst.

finely dispersed on Pt/C and appear to be deposited adjacent to the Pt. With continuously increasing the ALD cycles to 50, the TaO_x coating tended to form an over-coated thin layer on the Pt/C catalyst (Fig. 1(c)). This densely packed TaO_x layer would result in a large decrease of the active surface and thus negatively impact the activity. Therefore, it can be found that the ALD technology can be used to adjust the coverage and particle size of TaO_x to optimize the hybrid structure.

To examine the chemical species in the catalyst, XPS measurements were employed to study the composition of TaO_x deposited by ALD, and the results for 35ALD–TaO_x–Pt/C are displayed in Fig. 2. The XPS survey in Fig. 2(a) indicates the presence of Pt, Ta, O and C elements in the 35ALD–TaO_x–Pt/C catalyst. Fig. 2(b) illustrates the chemical environment of the Ta element by analyzing the Ta 4f spectrum. A couple of peaks located at binding energies of 28.5 ± 0.1 and 26.7 ± 0.1 eV are observed. These peaks are attributed to the responses of Ta $4f_{5/2}$ and Ta $4f_{7/2}$, respectively, belonging to the most stable Ta_2O_5 species. The other pair of Ta $4f_{5/2}$ and Ta $4f_{7/2}$ located at lower binding energies of 25.6 ± 0.1 and 23.7 ± 0.1 eV, respectively, is assigned as the TaO species. This result indicates that the Ta element in TaO_x exists in two types of chemical environments, *i.e.*, Ta_2O_5 and TaO, which consists of 96.3% and 3.7%, respectively. The dominant Ta_2O_5 species obviously resulted from the ALD of $Ta(OEt)_5$ and H_2O precursors. In the case of TaO, it could be expected that the oxygen can dissociate on the surface of Ta_2O_5 during high temperature annealing and thus result in the formation of a small amount of reduced TaO species.

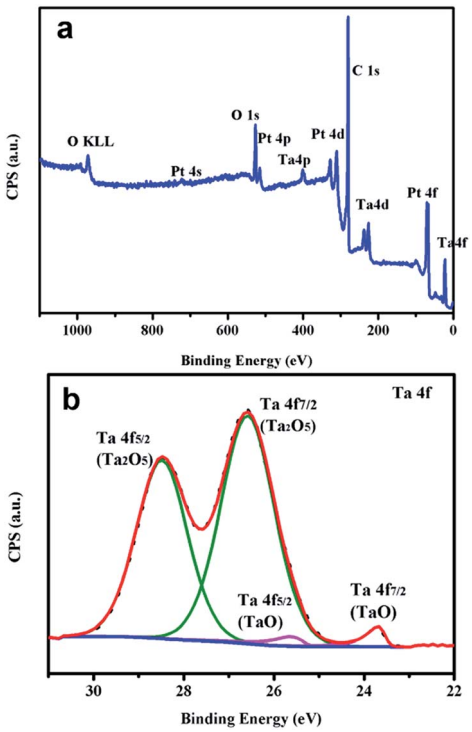

Fig. 2 (a) XPS spectra of survey scan and (b) Ta 4f XPS spectra obtained for 35ALD–TaO_x–Pt/C.

Electrocatalytic activity and durability

To determine the anchoring effect of TaO_x on the Pt/C catalyst, the electrochemical durability of the ALD–TaO_x–Pt/C catalysts was tested. The durability tests were performed by continuous triangle potential cycling between 0.6 V and 1.0 V (*vs.* RHE) in N_2-purged 0.10 M $HClO_4$ for 10 000 cycles to mimic the load-cycling experience during PEMFC operation. Fig. 3 illustrates the representative CV curves and ORR polarization curves recorded before and after ADT-10 000 for ALD–TaO_x–Pt/C and Pt/C catalysts. With continuous potential cycling, the CV curves of the Pt/C catalyst exhibited a pronounced reduction of total charge in the hydrogen underpotential deposition (HUPD) region, indicative of a reduction in Pt active surface area. The peak currents drop significantly with potential cycling, indicating severe catalyst degradation and activity loss of Pt/C. The losses of ECSA for different catalysts with the cycling numbers are plotted in Fig. 3(c) (the initial ECSA of Pt/C is considered as the baseline to calculate the normalized ECSA%) and the corresponding ECSA values at typical cycling numbers are summarized in Table S1.† As can be seen, the Pt/C catalyst experienced a significant ECSA decrease following the ADT (from 68.8 to 48.4 $m^2\ g^{-1}_{Pt}$ shown in Table S1†), losing 30% of its initial ECSA after ADT-10 000. The 15ALD–TaO_x–Pt/C catalyst demonstrates a slower degradation trend, losing 24.6% of its initial ECSA after ADT-10 000. While a small benefit in durability was observed for the 15ALD–TaO_x–Pt/C catalyst, the low coverage of the TaO_x anchors resulted in only limited improvement over the baseline. Conversely, the 35ALD–TaO_x–Pt/C catalyst actually shows an increased ECSA in the first 1000 cycles (from 60.6 up to 64.7 $m^2\ g^{-1}_{Pt}$), followed by a slight decrease to 62.7 $m^2\ g^{-1}_{Pt}$ after ADT-10 000 (with only 9.0% ECSA loss compared to the initial ECSA of Pt/C). These results reveal the superior durability of 35ALD–TaO_x–Pt/C compared to Pt/C and 15ALD–TaO_x–Pt/C catalysts. The increased ECSA in the initial ADT process suggests that a small percentage of the Pt surface may be covered by the TaO_x for the 35ALD–TaO_x–Pt/C catalyst, and the covered Pt surface can be activated by the potential cycling. It is hypothesized that the TaO_x particles located on the Pt surface exhibit a weak Pt–TaO_x interaction compared to the Pt–TaO_x–C triple-junctions, thus allowing them to redistribute during voltage cycling and expose additional Pt surface area. However, further increasing the TaO_x loading to 50 ALD cycles results in an 80% decrease in beginning of life (BOL) ECSA *vs.* Pt/C. This is consistent with the HRTEM results and confirms an almost over-coated Pt surface area by the TaO_x layer. Notably, during the ADT, the ECSA of the 50ALD–TaO_x–Pt/C catalyst gradually increased from 12.9 to 48.3 $m^2\ g^{-1}_{Pt}$, which further indicates that the TaO_x-covered Pt surface can be activated by the potential cycling. However, even after 10 000 ADT cycles, the increased ECSA of 50ALD–TaO_x–Pt/C is still much lower than that of 35ALD–TaO_x–Pt/C. Overall, the 35ALD–TaO_x–Pt/C catalyst with the triple-junction of TaO_x–Pt–C showed the most promise in terms of durability. Further catalytic activity toward ORR of this catalyst *vs.* Pt/C is provided below.

The LSV curves obtained under O_2-saturated $HClO_4$ for different catalysts before and after ADT-10 000 are shown in Fig. 3(d) and (e). The results indicate that 35ALD–TaO_x–Pt/C and

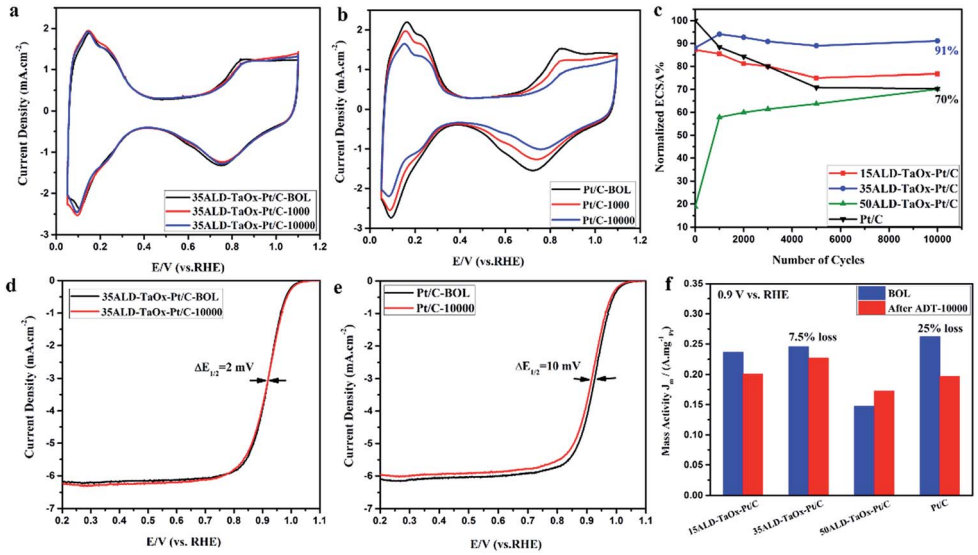

Fig. 3 Intermediate characterization CV curves of (a) 35ALD–TaO_x–Pt/C and (b) Pt/C catalysts during the load-cycling (0.6 V–1.0 V) durability tests in a N_2-saturated 0.1 M $HClO_4$ solution at a scan rate of 50 mV s^{-1}. (c) ECSA variation with cycling number for different catalysts cycled from 0.6 to 1.0 V. ORR polarization curves for (d) 35ALD–TaO_x–Pt/C and (e) Pt/C before and after ADT-10 000 (O_2, 1600 rpm, scan rate: 10 mV s^{-1}). (f) Mass activity of different catalysts at 0.9 V (*vs.* RHE) before and after ADT-10 000 (BOL stands for beginning of life before ADT).

Pt/C catalysts displayed an almost similar onset-potential of 1.075 V and 1.080 V, respectively, at BOL before ADT. The change in half-wave potential ($E_{1/2}$) after ADT-10 000 was used to evaluate the electrochemical durability. As shown in Fig. 3(d), the $E_{1/2}$ of 35ALD–TaO_x–Pt/C shifted from 0.920 V to 0.918 V with only a negligible degradation of 2 mV after ADT-10 000. However, for the Pt/C catalyst, a more severe degradation of 10 mV (from 0.920 V to 0.915 V) was observed after ADT-10 000. Based purely on the ECSA change, we would expect an $E_{1/2}$ loss of 7 mV calculated on the basis of Butler–Volmer kinetics.[56–58] The measured 10 mV loss is quite close to this, thus suggesting that the ECSA loss is primarily responsible for the activity loss. Furthermore, the ORR mass activities at 0.9 V before and after ADT-10 000 of the tested catalysts were calculated and are shown in Fig. 3(f) and Table S1.† Initially, the 35ALD–TaO_x–Pt/C catalyst exhibited comparable mass activity (0.246 A mg^{-1}_{Pt}) to that of Pt/C (0.262 A mg^{-1}_{Pt}). After ADT-10 000, the mass activity of 35ALD–TaO_x–Pt/C at 0.9 V is 0.227 A mg^{-1}_{Pt} (only 7.5% loss), which is much higher than that of the Pt/C catalyst (0.197 A mg^{-1}_{Pt}). The high durability of the 35ALD–TaO_x–Pt/C catalyst further confirms the anchoring effect of TaO_x.

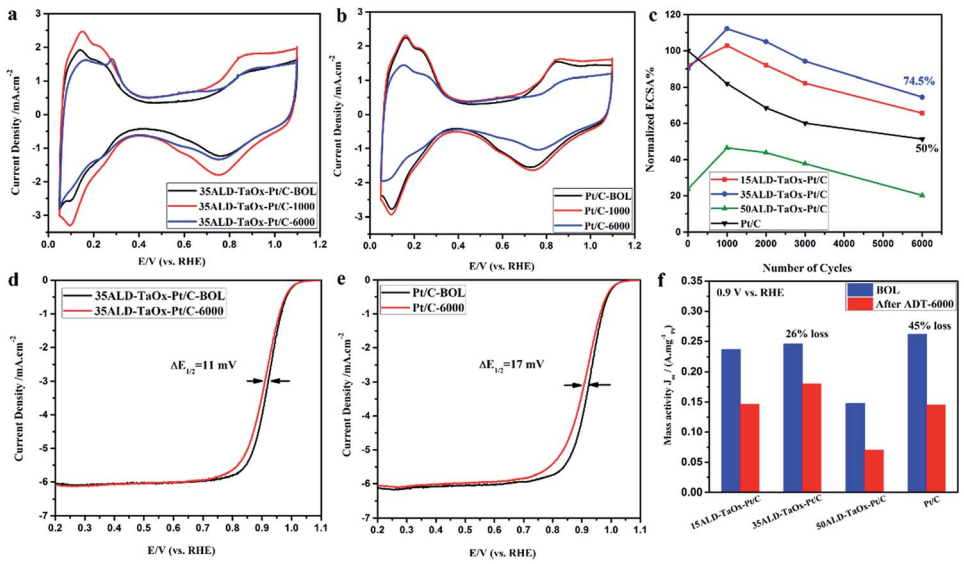

Fig. 4 Intermediate characterization CV curves of (a) 35ALD–TaO_x–Pt/C and (b) Pt/C catalyst during the start-up/shut-down (1.0 V–1.6 V) durability tests in a N_2-saturated 0.1 M $HClO_4$ solution at a scan rate of 100 mV s^{-1}. (c) Variation of ECSA with cycling number for different catalysts cycled from 1.0 to 1.6 V. ORR polarization curves for (d) 35ALD–TaO_x–Pt/C and (e) Pt/C catalyst before and after cycling between 1.0 V and 1.6 V (O_2, 1600 rpm, scan rate: 10 mV s^{-1}). (f) Mass activity of different catalysts at 0.9 V (*vs.* the RHE) before and after ADT-6000.

The process of Pt crystal migration and coalescence directly impacts ECSA at a low potential (<1.0 V *vs.* RHE).[59–61] However, at high potentials (>1.1 V *vs.* RHE), the carbon support is prone to oxidation or corrosion.[62,63] Carbon corrosion can lead to physical detachment of Pt NPs, resulting in complete catalytic activity loss for the detached Pt NPs.[60] This is especially problematic during partial fuel starvation[64] or PEMFC start-up/shutdown events when the cell voltage can reach up to 1.5 V or higher.[65,66] Thus, additional potential cycling experiments were carried out in a potential range of 1.0–1.6 V *vs.* RHE for 6000 cycles at a scan rate of 100 mV s^{-1}, to mimic the experience of the cathode catalyst during PEMFC start-up/shutdown. Fig. 4(a) and (b) show the changes of CV curves for different catalysts during ADT-6000. The normalized ECSA variations with cycling numbers are shown in Fig. 4(c) and the corresponding ECSA values at typical cycling numbers are summarized in Table S2.† For the Pt/C catalyst, the ECSA recorded after ADT-6000 is just 50% maintained (decreased from 66.4 to 34.0 m^2 g^{-1}_{Pt}), the $E_{1/2}$ experienced a 17.0 mV degradation and the mass activity at 0.9 V exhibited 45.0% loss (dropped from 0.262 to 0.145 A mg^{-1}_{Pt}) after ADT-6000 (Fig. 4(d)–(f)). However, the catalytic activity of 35ALD–TaO_x–Pt/C increased with potential cycling and revealed the highest ECSA after 1000 potential cycles. It retains 74.5% of the initial ECSA after ADT-6000 and is 24.5% higher than that of Pt/C. Additionally, the 35ALD–TaO_x–Pt/C catalyst displayed a 24.0% higher mass activity at 0.9 V (0.180 A mg^{-1}_{Pt}) than Pt/C (0.145 A mg^{-1}_{Pt}) after ADT-6000. This confirmed that 35ALD–TaO_x–Pt/C showed a much better stability than Pt/C even under the harsh cycling conditions. During potential cycling between 1.0 V and 1.6 V (*vs.* the RHE), the Pt/C and 35ALD–TaO_x–Pt/C catalysts showed a notable increase in the capacitive double layer region (0.4 V–0.6 V). This is due to the carbon oxidation reaction which leads to the formation of pseudo-capacitive groups and/or micropores on the carbon surface. The carbon oxidation decreases the amount of carbon available to support Pt, resulting in detachment of the Pt NPs and decrease in the active surface area.[10] From 0 to 1000 cycles, the ECSA of Pt/C exhibited a drastic decrease (from 66.4 to 54.5 m^2. g^{-1}_{Pt}) with the increased double layer capacity, which indicated that detachment of Pt NPs occurs during the carbon corrosion process. However, the ECSA of 35ALD–TaO_x–Pt/C exhibited no degradation after 1000 potential cycles. This is because the TaO_x anchors played a significant role in stabilizing Pt NPs and effectively prevented the detachment of the Pt NPs under the severe carbon oxidation and corrosion conditions.

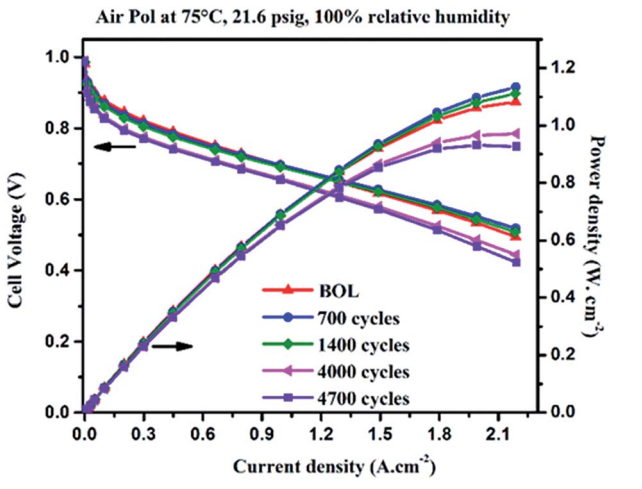

Fig. 5 H_2–air fuel cell polarization curves for MEA using 35ALD–TaO_x–Pt/C as the cathode after different aging cycles with the Pt loading on the anode and cathode of 0.1 and 0.15 mg cm^{-2}, respectively.

PEMFC single cell performance

Based on the electrochemical results, potential cycling between 0.6 V and 1.0 V *vs.* the RHE was performed on MEA to further study the single cell durability performance. The current–voltage and corresponding current–power density curves for the MEA after different ADT cycles are shown in Fig. 5. Under conditions of high temperature and humidity (75 °C, 100% RH), the MEA exhibited highly stable performance in the long-term durability test. As shown in Fig. 5, the cell voltage increased with the potential cycling and revealed the highest cell voltage of 653 mV at a high current density (1.3 A cm^{-2}) after 700 potential cycles, with only 40 mV voltage loss after 4700 ADT cycles (~120 h), which indicated a highly stable catalyst performance. Furthermore, the beginning peak power density was 1.08 W cm^{-2}, and it increased to 1.13 W cm^{-2} and 1.11 W cm^{-2} after 700 and 1400 ADT cycles, respectively. Even after 4700 ADT cycles, the peak power density is maintained at 0.95 W. cm^{-2} with only 12% loss. This shows much better durability than the commercial Pt/C catalyst reported in the literature (with ≥27% power loss after 100 h or less aggressive accelerated durability test).[67–70] The cathode catalyst was collected from the MEA after accelerate cycling, and the morphology of the 35ALD–TaO_x–Pt/C catalyst before and after ADT was examined by TEM and XRD patterns. Fig. S4† shows that the Pt NPs were uniformly distributed on the carbon support after 4700 ADT cycles and the average particle size was 3.9 ± 0.5 nm. The uniform distribution and small change in Pt particle size suggest that the TaO_x was successful in stabilizing the Pt catalyst.

The mechanism of the dramatically enhanced stability could be related to the triple-junction structure of the TaO_x-anchored Pt NPs on the carbon support. First, Pt NPs in the commercial Pt/C catalyst are easy to migration and coalescence, due to the relatively weak interactions between Pt NPs and the carbon support, which is a major factor for catalyst degradation during PEMFC operation. For 35ALD–TaO_x–Pt/C with TaO_x-anchored Pt NPs, the migration and coalescence process might be alleviated due to the construction of triple junctions of TaO_x–Pt–C. These strong interactions enhance the catalyst stability and minimize the ECSA loss, as illustrated in Scheme 2(a). Furthermore, as previously reported, carbon corrosion often occurs in the presence of the Pt catalyst and at high potential (>1.5 V), especially under the conditions of PEMFC fuel starvation and start-up/shutdown. Thus, for the Pt/C catalyst, Pt NPs detach from the support when the carbon is oxidized, resulting

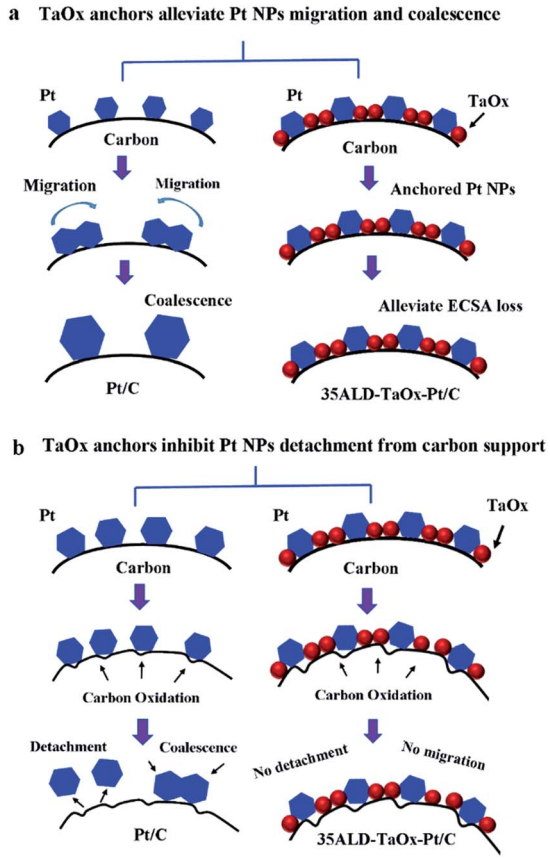

Scheme 2 Schematic of the stability mechanism of the 35ALD–TaO_x–Pt/C catalyst with triple junctions of TaO_x–Pt–C. (a) TaO_x alleviating Pt NPs migration and coalescence; (b) TaO_x inhibiting the detachment and coalescence of Pt NPs.

in loss of catalytic activity. By contrast for 35ALD–TaO_x–Pt/C catalyst, Pt NPs remain anchored on the carbon surface even when the carbon support is partly corroded. The strong triple-junction structure will efficiently prevent the detachment of Pt NPs and enhance the Pt catalyst stability. The detailed processes are illustrated in Scheme 2(b).

Conclusion

In summary, metal oxide (TaO_x) modified commercial Pt/C catalysts with TaO_x-anchored Pt NPs were prepared by an area-selective atomic layer deposition method. After heat removal of the protective agent, the TaO_x-anchored Pt NPs with a unique triple-junction structure were formed. The TaO_x particles could tightly immobilize Pt NPs on the carbon support and played a significant role in stabilizing the Pt catalyst through the metal oxide anchoring effect. The electrochemical data revealed that the TaO_x-anchored Pt catalyst with 35 ALD cycles of TaO_x deposition displayed comparable catalytic activity to the commercial Pt/C catalyst. Significantly, the 35ALD–TaO_x–Pt/C catalyst exhibited superior long-term stability of both electrochemical surface area and ORR mass activity in comparison to Pt/C. Furthermore, MEA durability tests show that the anchored 35ALD–TaO_x–Pt/C catalyst exhibits good long-term stability with only 12% power density loss after 120 h aging. The excellent stability of 35ALD–TaO_x–Pt/C should be ascribed to the strong anchoring effect of TaO_x towards Pt NPs which hinders the migration, coalescence and detachment of Pt NPs from the support. Therefore, the construction of TaO_x-anchored Pt NPs can offer a persuasive approach towards increasing the lifetime of the catalysts applied in PEMFCs.

Acknowledgements

This research was supported by Ballard Power Systems Inc., Catalysis Research for Polymer Electrolyte Fuel Cells (CaRPE-FC), Natural Sciences and Engineering Research Council of Canada (NSERC), Canada Research Chair (CRC) Program, Canada Foundation for Innovation (CFI), Ontario Research Fund (ORF), Automotive Partnership of Canada, and the University of Western Ontario. Z. Song was supported by the Chinese Scholarship Council.

Notes and references

1 M. K. Debe, *Nature*, 2012, **486**, 43–51.
2 M. Jacobson, W. Colella and D. Golden, *Science*, 2005, **308**, 1901–1905.
3 R. F. Service, *Science*, 2002, **296**, 1222–1224.
4 W. Yu, M. D. Porosoff and J. G. Chen, *Chem. Rev.*, 2012, **112**, 5780–5817.
5 C. Cui, L. Gan, M. Heggen, S. Rudi and P. Strasser, *Nat. Mater.*, 2013, **12**, 765–771.
6 L. Zhang, L. T. Roling, X. Wang, M. Vara, M. Chi, J. Liu, S.-I. Choi, J. Park, J. A. Herron, Z. Xie, M. Mavrikakis and Y. Xia, *Science*, 2015, **349**, 412–416.
7 C. Chen, Y. Kang, Z. Huo, Z. Zhu, W. Huang, H. L. Xin, J. D. Snyder, D. Li, J. A. Herron, M. Mavrikakis, M. Chi, K. L. More, Y. Li, N. M. Markovic, G. A. Somorjai, P. Yang and V. R. Stamenkovic, *Science*, 2014, **343**, 1339–1343.
8 M. Li, Z. Zhao, T. Cheng, A. Fortunelli, C. Y. Chen, R. Yu, Q. Zhang, L. Gu, B. V. Merinov and Z. Lin, *Science*, 2016, **354**, 1414–1419.
9 N. Cheng, M. N. Banis, J. Liu, A. Riese, S. Mu, R. Li, T.-K. Sham and X. Sun, *Energy Environ. Sci.*, 2015, **8**, 1450–1455.
10 Y. Shao, G. Yin and Y. Gao, *J. Power Sources*, 2007, **171**, 558–566.
11 A. Brouzgou, S. Song and P. Tsiakaras, *Appl. Catal., B*, 2012, **127**, 371–388.
12 X. Yu and S. Ye, *J. Power Sources*, 2007, **172**, 145–154.
13 Y. Shao-Horn, W. Sheng, S. Chen, P. Ferreira, E. Holby and D. Morgan, *Top. Catal.*, 2007, **46**, 285–305.
14 S. Sun, F. Jaouen and J. P. Dodelet, *Adv. Mater.*, 2008, **20**, 3900–3904.
15 Z. Chen, M. Waje, W. Li and Y. Yan, *Angew. Chem., Int. Ed.*, 2007, **46**, 4060–4063.
16 S. Sun, D. Yang, D. Villers, G. Zhang, E. Sacher and J.-P. Dodelet, *Adv. Mater.*, 2008, **20**, 571–574.
17 G. Zhang, S. Sun, M. Cai, Y. Zhang, R. Li and X. Sun, *Sci. Rep.*, 2013, **3**, 1–8.

18 S. Guo, S. Dong and E. Wang, *ACS Nano*, 2010, **4**, 547–555.
19 Z. Peng, H. You and H. Yang, *ACS Nano*, 2010, **4**, 1501–1510.
20 D. Wang, H. L. Xin, R. Hovden, H. Wang, Y. Yu, D. A. Muller, F. J. DiSalvo and H. D. Abruña, *Nat. Mater.*, 2013, **12**, 81–87.
21 V. R. Stamenkovic, B. Fowler, B. S. Mun, G. Wang, P. N. Ross, C. A. Lucas and N. M. Marković, *Science*, 2007, **315**, 493–497.
22 V. R. Stamenkovic, B. S. Mun, M. Arenz, K. J. Mayrhofer, C. A. Lucas, G. Wang, P. N. Ross and N. M. Markovic, *Nat. Mater.*, 2007, **6**, 241–247.
23 D. Geng, Y. Hu, Y. Li, R. Li and X. Sun, *Electrochem. Commun.*, 2012, **22**, 65–68.
24 S. Takenaka, H. Miyamoto, Y. Utsunomiya, H. Matsune and M. Kishida, *J. Phys. Chem. C*, 2014, **118**, 774–783.
25 J. Jones, H. Xiong, A. T. DeLaRiva, E. J. Peterson, H. Pham, S. R. Challa, G. Qi, S. Oh, M. H. Wiebenga, X. I. Pereira Hernández, Y. Wang and A. K. Datye, *Science*, 2016, **353**, 150–154.
26 X. Tian, J. Luo, H. Nan, H. Zou, R. Chen, T. Shu, X. Li, Y. Li, H. Song and S. Liao, *J. Am. Chem. Soc.*, 2016, **138**, 1575–1583.
27 T. Fujigaya and N. Nakashima, *Adv. Mater.*, 2013, **25**, 1666–1681.
28 D. He, K. Cheng, H. Li, T. Peng, F. Xu, S. Mu and M. Pan, *Langmuir*, 2012, **28**, 3979–3986.
29 D. He, S. Mu and M. Pan, *Carbon*, 2011, **49**, 82–88.
30 K. Cheng, Z. Kou, J. Zhang, M. Jiang, H. Wu, L. Hu, X. Yang, M. Pan and S. Mu, *J. Mater. Chem. A*, 2015, **3**, 14007–14014.
31 R. Kou, Y. Shao, D. Mei, Z. Nie, D. Wang, C. Wang, V. V. Viswanathan, S. Park, I. A. Aksay and Y. Lin, *J. Am. Chem. Soc.*, 2011, **133**, 2541–2547.
32 N. Cheng, J. Liu, M. N. Banis, D. Geng, R. Li, S. Ye, S. Knights and X. Sun, *Int. J. Hydrogen Energy*, 2014, **39**, 15967–15974.
33 P. Lu, C. T. Campbell and Y. Xia, *Nano Lett.*, 2013, **13**, 4957–4962.
34 A. Kumar and V. Ramani, *ACS Catal.*, 2014, **4**, 1516–1525.
35 S. Shanmugam and A. Gedanken, *Small*, 2007, **3**, 1189–1193.
36 J. Seo, D. Cha, K. Takanabe, J. Kubota and K. Domen, *ACS Catal.*, 2013, **3**, 2181–2189.
37 J. Y. Kim, T.-K. Oh, Y. Shin, J. Bonnett and K. S. Weil, *Int. J. Hydrogen Energy*, 2011, **36**, 4557–4564.
38 T. Ushikubo, *Catal. Today*, 2000, **57**, 331–338.
39 A. Bonakdarpour, R. Löbel, S. Sheng, T. Monchesky and J. Dahn, *J. Electrochem. Soc.*, 2006, **153**, A2304–A2313.
40 J. Seo, D. Cha, K. Takanabe, J. Kubota and K. Domen, *Chem. Commun.*, 2012, **48**, 9074–9076.
41 J. Seo, D. Cha, K. Takanabe, J. Kubota and K. Domen, *Phys. Chem. Chem. Phys.*, 2014, **16**, 895–898.
42 J. Seo, D. H. Anjum, K. Takanabe, J. Kubota and K. Domen, *Electrochim. Acta*, 2014, **149**, 76–85.
43 J. Seo, L. Zhao, D. Cha, K. Takanabe, M. Katayama, J. Kubota and K. Domen, *J. Phys. Chem. C*, 2013, **117**, 11635–11646.
44 Z. Awaludin, J. G. S. Moo, T. Okajima and T. Ohsaka, *J. Mater. Chem. A*, 2013, **1**, 14754–14765.
45 J. Lu, B. Fu, M. C. Kung, G. Xiao, J. W. Elam, H. H. Kung and P. C. Stair, *Science*, 2012, **335**, 1205–1208.
46 C. Marichy, M. Bechelany and N. Pinna, *Adv. Mater.*, 2012, **24**, 1017–1032.
47 J. Lu, K.-B. Low, Y. Lei, J. A. Libera, A. Nicholls, P. C. Stair and J. W. Elam, *Nat. Commun.*, 2014, **5**, 3264.
48 J. Lu, J. W. Elam and P. C. Stair, *Acc. Chem. Res.*, 2013, **46**, 1806–1815.
49 R. H. A. Ras, E. Sahramo, J. Malm, J. Raula and M. Karppinen, *J. Am. Chem. Soc.*, 2008, **130**, 11252–11253.
50 R. Chen and S. F. Bent, *Adv. Mater.*, 2006, **18**, 1086–1090.
51 N. Cheng, M. N. Banis, J. Liu, A. Riese, X. Li, R. Li, S. Ye, S. Knights and X. Sun, *Adv. Mater.*, 2015, **27**, 277–281.
52 J. Liu, M. N. Banis, X. Li, A. Lushington, M. Cai, R. Li, T.-K. Sham and X. Sun, *J. Phys. Chem. C*, 2013, **117**, 20260–20267.
53 K. Kukli, M. Ritala and M. Leskelä, *J. Electrochem. Soc.*, 1995, **142**, 1670–1675.
54 S. Trasatti and O. Petrii, *Pure Appl. Chem.*, 1991, **63**, 711–734.
55 A. Riese, D. Banham, S. Ye and X. Sun, *J. Electrochem. Soc.*, 2015, **162**, F783–F788.
56 D. A. Noren and M. A. Hoffman, *J. Power Sources*, 2005, **152**, 175–181.
57 W. Sheng, H. A. Gasteiger and Y. Shao-Horn, *J. Electrochem. Soc.*, 2010, **157**, B1529–B1536.
58 J. Wang, N. Markovic and R. Adzic, *J. Phys. Chem. B*, 2004, **108**, 4127–4133.
59 M. S. Wilson, F. H. Garzon, K. E. Sickafus and S. Gottesfeld, *J. Electrochem. Soc.*, 1993, **140**, 2872–2877.
60 Y. Shao-Horn, P. Ferreira, D. Morgan, H. Gasteiger and R. Makharia, *ECS Trans.*, 2006, **1**, 185–195.
61 G. Gruver, R. Pascoe and H. Kunz, *J. Electrochem. Soc.*, 1980, **127**, 1219–1224.
62 R. Makharia, S. Kocha, P. Yu, M. A. Sweikart, W. Gu, F. Wagner and H. A. Gasteiger, *ECS Trans.*, 2006, **1**, 3–18.
63 L. Castanheira, W. O. Silva, F. H. Lima, A. Crisci, L. Dubau and F. d. r. Maillard, *ACS Catal.*, 2015, **5**, 2184–2194.
64 A. Taniguchi, T. Akita, K. Yasuda and Y. Miyazaki, *J. Power Sources*, 2004, **130**, 42–49.
65 J. Durst, A. Lamibrac, F. Charlot, J. Dillet, L. F. Castanheira, G. Maranzana, L. Dubau, F. Maillard, M. Chatenet and O. Lottin, *Appl. Catal., B*, 2013, **138**, 416–426.
66 J. Dillet, D. Spernjak, A. Lamibrac, G. Maranzana, R. Mukundan, J. Fairweather, S. Didierjean, R. Borup and O. Lottin, *J. Power Sources*, 2014, **250**, 68–79.
67 D. Y. Chung, S. W. Jun, G. Yoon, S. G. Kwon, D. Y. Shin, P. Seo, J. M. Yoo, H. Shin, Y.-H. Chung and H. Kim, *J. Am. Chem. Soc.*, 2015, **137**, 15478–15485.
68 Y. Jeon, H. Na, H. Hwang, J. Park, H. Hwang and Y.-g. Shul, *Int. J. Hydrogen Energy*, 2015, **40**, 3057–3067.
69 Z.-M. Zhou, Z.-G. Shao, X.-P. Qin, X.-G. Chen, Z.-D. Wei and B.-L. Yi, *Int. J. Hydrogen Energy*, 2010, **35**, 1719–1726.
70 Z. Xia, S. Wang, L. Jiang, H. Sun, S. Liu, X. Fu, B. Zhang, D. Sheng Su, J. Wang and G. Sun, *Sci. Rep.*, 2015, **5**, 16100.